ACS Catalysis

pubs.acs.org/acscatalysis Research Article

# Identifying Support Effects in Au-Catalyzed CO Oxidation

Zachary R. Mansley, Ryan J. Paull, Louisa Savereide, Scott Tatro, Emily P. Greenstein, Abha Gosavi, Emily Cheng, Jianguo Wen, Kenneth R. Poeppelmeier, Justin M. Notestein, and Laurence D. Marks*

Cite This: ACS Catal. 2021, 11, 11921−11928 Read Online

ACCESS | Metrics & More | Article Recommendations | Supporting Information

**ABSTRACT:** Some catalytic oxide supports are more equal than others, with numerous variable properties ranging from crystal symmetry to surface chemistry and electronic structure. As a consequence, it is often very difficult to determine which of these act as the driver of performance changes observed in catalysis. In this work, we hold many of these variable properties constant with structurally similar $LnScO_3$ (Ln = La, Sm, and Nd) nanoparticle supports with cuboidal shapes and a common Sc-rich surface termination. Using CO oxidation over supported Au nanoparticles as a probe reaction, we observe higher activation energy and a slower rate using $NdScO_3$ as the support material. This change is found to correlate to the strength of $CO_2$ binding to the support surface, identified by temperature-programmed desorption measurements. The change is due to differences in the 4f electrons of the lanthanide cations, the cations' Lewis acidity, and the inductive effect they impose.

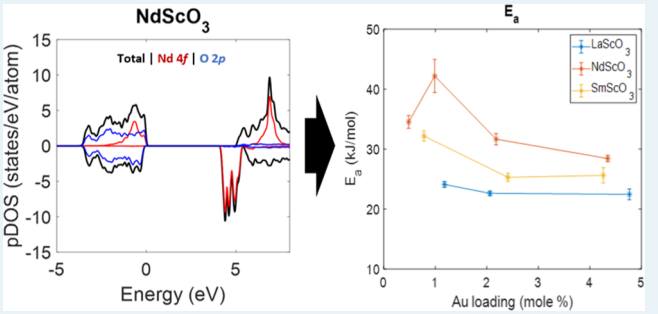


KEYWORDS: *support effects, electronic structure, electron microscopy, DFT, surfaces, thermodynamics*



## INTRODUCTION

Oxide-supported noble metal nanoparticles have been utilized in catalysis for decades.[1−5] Supporting metal nanoparticles on an oxide has numerous benefits, notably the reduction in sintering and the ability to change the catalytic behavior of metals by adjusting the support.[6−9] The latter comes about due to the introduction of a second material to the catalytic system, and while it can be convenient to view supports as inactive, the interaction between the metal nanoparticle and support can be very important. This contact can have significant impacts on catalytic performance,[10,11] and the joint optimization of the ideal metal nanoparticle on the ideal support will lead to the best catalytic performance.

However, the use of a composite material system introduces additional independent variables. Even neglecting support options such as metal−oxide frameworks and mesoporous microstructures, varied solid oxide support materials have different chemistries, crystal symmetries, surface properties, and electronic structures—an incomplete list. This is further complicated by the presence of an interface with the supported metal, where epitaxy,[12] particle adhesion,[13] and electronic band bending[14] change both the static and dynamic behavior of the nanoparticles. As a result, when a given catalyst performs differently on various supports, it is incredibly difficult to isolate the root cause as so much is changing from support to support. For example, if the active site sits at the interface between the catalyst and support, comparing alumina and titania would be complicated by the fundamental differences in chemistry and structure between the two.

Important efforts have been made to separate these factors by various methods, with varying degrees of success. For instance, Schlapka *et al.* attempted to disentangle the chemical/electronic substrate interaction from mechanical strain in Pt on Ru(0001) through layered film growth and electronic structure calculations.[15] This worked, though only for a select number of atomic layers in which the substrate is screened, but strain relaxation is yet to occur. Similarly, researchers have sought to remove the substrate effect entirely and strain metal films backed by polymers.[16] However, microstructural effects from strain and local delamination may play a complicating role at higher strains,[17] limiting the accessible window of study. A slightly different approach has also been taken where the surface termination and/or the dominant surface facets of the support have been changed, for instance.[12,13,18−21]

We aim to minimize these complicating factors using a series of structurally similar $LnScO_3$ supports (Ln = La, Nd, and Sm). These supports share the *Pbnm* orthorhombic perovskite structure,[22,23] a Sc-rich surface termination,[24−27] have similar electronic structures,[28−30] and are a good lattice match for many noble metal catalysts in terms of the pseudocubic unit

Received: July 13, 2021




https://doi.org/10.1021/acscatal.1c03156
ACS Catal. 2021, 11, 11921−11928

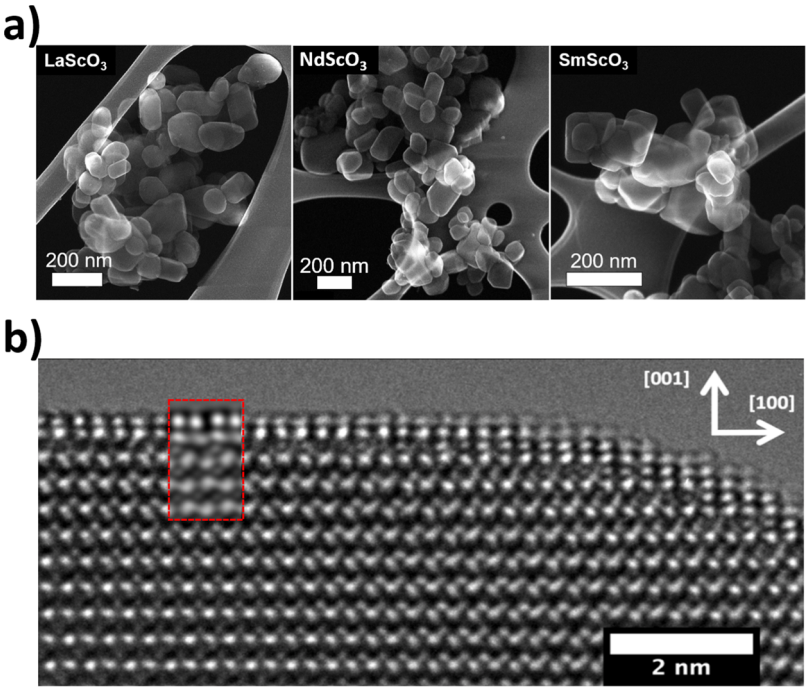


**Figure 1.** Secondary electron images of the different $LnScO_3$ support nanoparticles (a), with an aberration-corrected profile image of the surface of $SmScO_3$ (b). Highlighted in red is an inset multislice simulation generated using the MacTempasX program based on a double layer surface structure.[24,26,27]

cell. As a result, many of the aforementioned independent variables, such as structural symmetry and surface chemistry, are close to identical across the series, and catalytic effects stemming from any changes to the support can be isolated and identified.

To probe if any catalytic effects arise from changing the $LnScO_3$ support, a test case of CO oxidation over supported Au nanoparticles is used herein. Supported Au nanoparticles are known to be good catalysts for this reaction,[31] and the lack of side reactions and multiple intermediate phases allows for easier analysis and attribution of catalytic performance to fundamental material properties. By thoroughly characterizing the catalyst system to identify similarities and differences across the series of samples and comparing these tracked properties to the behavior of the catalyst in the reaction, we can identify either correlation or independence. In this study, we show that the behavior of Au and the active site shows little variability across the supports, while the basicity of the support surface, that is, the ability to donate electrons to the reaction species, is the property of significance in terms of determining the energy barrier and the rate of reaction in this system.

## METHODS

Oxide supports of $LaScO_3$, $NdScO_3$, and $SmScO_3$ were synthesized using a hydro-sauna method that produces faceted nanoparticles.[32,33] Au was then deposited on the substrates using a deposition−precipitation method as outlined in studies by Zanella *et al.*[34] TEM characterization was carried out using the Argonne Chromatic Aberration-corrected transmission electron microscope (ACAT) operated at 200 kV for observing the surface reconstructions and nanoparticle structure, and a FEI Talos operated at 200 kV in both moderate-angle and high-angle annular dark-field modes was used to measure particle sizes. Additionally, some microscopy was performed using a JEOL ARM300F at 300 kV for nanoparticle morphology determination, and a Hitachi HD-2300 scanning transmission electron microscope at 200 kV was used to observe the morphology of the support using secondary electrons. Image simulations were performed using the MacTempasX software package using typical ACAT working conditions (<10 $\mu$m Cs, 40 nm focal spread) and the previously reported surface structure with atomic positions minimized from DFT calculations.[24−27]

The bare supports were also characterized with BET analysis using a Micromeritics 3Flex to determine the surface area, and $CO_2$ temperature-programmed desorption measurements coupled with downstream mass spectrometry (TPD-MS) were obtained using an AMI-200 and a SRS Universal Gas Analyzer 100 to determine relative $CO_2$ binding strength. The TPD-MS samples were heated to 350 °C for 3 h and then pretreated with $CO_2$ at 50 °C for 20 min before heating to 800 °C at a ramp rate of 10 °C/min with simultaneous data collection.

To determine the loading of Au, the samples were analyzed with either ICP-optical emission spectrometry (ICP-OES) or MS, using a Thermo iCAP 7600 ICP-OES instrument operated in axial mode or a Thermo iCAP Q ICP−MS instrument operated in kinetic energy discrimination mode. The samples were digested in HCl and then diluted to a 5% concentration for analysis. All loadings are reported in mole % due to the slightly different molar weights of the supports, which are 18−24% higher than the weight % on a given sample.

To test CO oxidation, the samples were prepared by mixing 10−15 mg of a catalyst with 400 mg of quartz ($SiO_2$) sand from Sigma-Aldrich and dried for 90 min at 150 °C in a mixture of 40 sccm of oxygen and 10 sccm of helium. The samples were then brought up to 250 °C and held for 5 h under 40 sccm of oxygen, 10 sccm helium, and 20 sccm of CO to assess catalyst stability. The same gas composition was used


https://doi.org/10.1021/acscatal.1c03156
ACS Catal. 2021, 11, 11921−11928

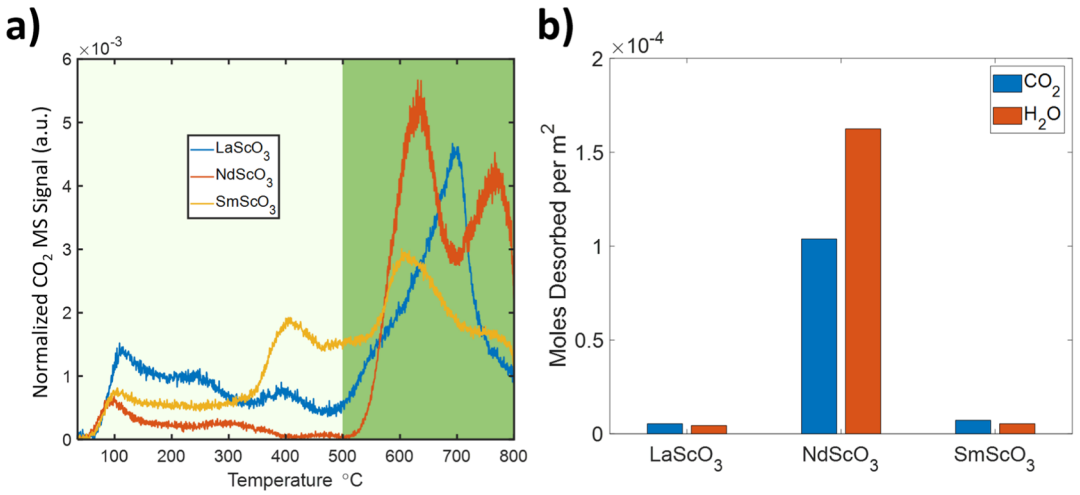


**Figure 2.** Variation of the temperature dependence of the carbon dioxide desorption on the different substrates. (a) $CO_2$ TPD-MS results of the blank supports normalized by the integrated $CO_2$ desorption. The plot has been divided between low- and high-temperature desorption regimes for analysis in Table 1. Total moles of $CO_2$ and $H_2O$ are shown in (b) normalized to the support surface area. As shown, $NdScO_3$ has significantly less low-temperature desorption, implying stronger $CO_2$ binding. All supports have surface areas of approximately 6 $m^2/g$.

to assess the catalytic performance of the samples at 275 °C for 20 min. The samples were then measured for 15 min at 125, 150, 175, and 200 °C in order, with the gases bypassing the main reactor during temperature changes. Flow rates were controlled using a Camile data acquisition and control system, and the products were measured using a Pfeiffer Themostar Q200 mass spectrometer.

DFT calculations were performed for the bulk materials using the all-electron augmented plane wave + local orbitals WIEN2K package[35,36] with on-site hybrids[37,38] and the PBEsol functional.[39] As discussed previously,[24−26,30] the $LnScO_3$ system is adequately described using on-site hybrid fractions of 0.38, 0.50, and 0.80 for the Ln 4f, Ln 5d, and Sc 3d orbitals, respectively, and muffin-tin radii of 2.02, 1.82, and 1.68 for the Ln, Sc, and O atoms, respectively. Note that the lanthanide 4f electrons are included in the valence band in these calculations, not forced into the core; previous work[25,30] clearly indicated that this matters.

## RESULTS

Figure 1 shows secondary electron images of as-synthesized bare $LnScO_3$ support particles, with an aberration-corrected profile view image of $SmScO_3$, revealing the double layer surface structure and a multislice simulation inset. The support particles primarily form faceted, cuboidal shapes that expose the pseudocubic (100) planes [note: the *Pbnm* $LnScO_3$ unit cell contains 2 pseudocubic units defined by the {110} and (002) planes]. The structure of the (110) surface has been previously studied,[24−27,40−43] and the double layer structure observed in Figure 1b agrees well with the results of those studies. Analysis by BET yields surface areas of approximately 6 $m^2/g$ for all of the supports. This corresponds to an average side length of approximately 150 nm, assuming a perfectly cubic morphology.

To further characterize the bare supports, the results of $CO_2$ desorption are shown in Figure 2 and Table 1. The $LaScO_3$ and $SmScO_3$ supports desorb 30−40% of $CO_2$ in the low-temperature regime below 500 °C, whereas the $NdScO_3$ support binds the $CO_2$ molecules to the surface more strongly where 90% of the adsorbed $CO_2$ is desorbed at high temperatures. Between 125 and 275 °C, the range probed during CO oxidation experiments, $NdScO_3$ retains the most $CO_2$ on the surface, followed by $SmScO_3$, then $LaScO_3$. In addition to binding a significant population of $CO_2$ more strongly than the other supports, the $NdScO_3$ support also binds a larger overall amount of adsorbates, as shown in Figure 2b. The $H_2O$ signal is the result of $H_2O$ that remained on the surface following the 350 °C pretreatment step.

**Table 1. Comparison of $CO_2$ Binding Populations on $LnScO_3$**

| | $LaScO_3$ (%) | $NdScO_3$ (%) | $SmScO_3$ (%) |
|---|---|---|---|
| weakly bound[a] | 34 | 10 | 39 |
| strongly bound[b] | 66 | 90 | 61 |

[a]The weak binding regime is defined as below 500 °C. [b]The strong binding regime is between 500 and 800 °C. We note that any choice of delimiting temperature between these regimes above ∼100 °C results in $NdScO_3$ having the highest proportion of strongly bound $CO_2$.

Au was deposited on the supports with measured loadings of 0.18 to 4.77 mol % and then catalytically tested as described in the previous section. The supported Au nanoparticles had both single-crystalline and polycrystalline morphologies, as shown in Figure 3b, with most of the polycrystals exhibiting a twinned structure; the occurrence of twins in gold nanoparticles is very common, see refs 44−47 as well as references therein. Of relevance later, there was no notable difference in the height to width ratio of the particles on the different substrates, that is, the Winterbottom shape[48] and its equivalent for twinned particles,[49] indicating that the free energy of the interfaces on the substrates had minimal dependence on both particle morphology and the lanthanide.[13,47−49]

Figure 3a shows the average size of both the as-deposited (blue) and the post-CO oxidation (orange) Au nanoparticles on each support, with detailed statistics in Supporting Information, including the density of Au nanoparticles on the support surface (note that the very low loadings were not deposited on $NdScO_3$; this is also discussed in Supporting Information). Here it is evident that depending on the initial size, the Au nanoparticles could undergo two routes of sintering. When the initial size is very small and the Au


https://doi.org/10.1021/acscatal.1c03156
ACS Catal. 2021, 11, 11921−11928

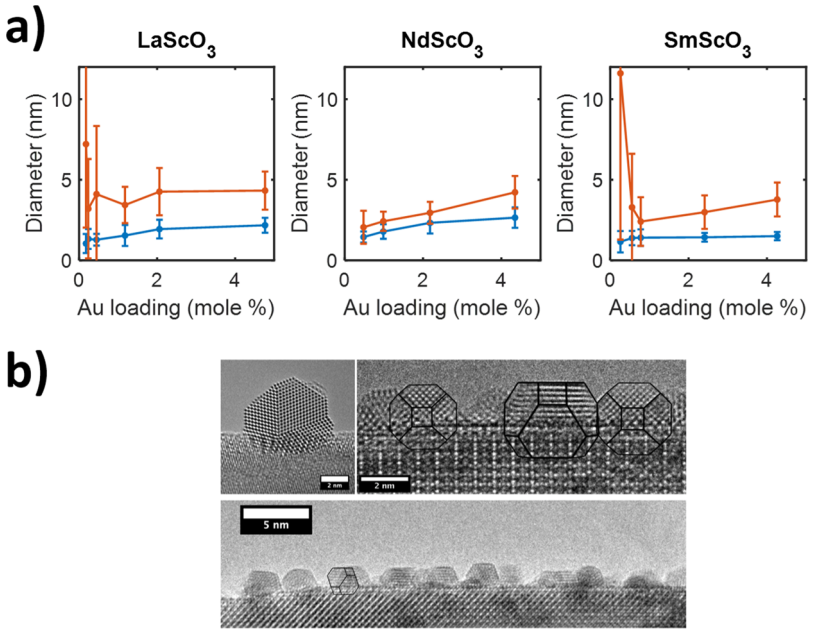


**Figure 3.** Average diameters of Au nanoparticles on the various supports with as-deposited sizes in blue and after testing sizes in orange. Error bars show the standard deviations of each data set. (b) Aberration-corrected TEM images of the as-deposited supported nanoparticles on $NdScO_3$ (top right) and $SmScO_3$ (bottom) substrates, including multiply twinned particles (MTPs) and single crystals with varying orientations. Note that with the exception of the particle shown in the top left, all of the nanoparticles have a similar adhesion on the substrate regardless of the support, morphology, or orientation. The larger, twinned particle (decahedral MTP) in the top left is characteristic of the runaway sintering samples, though they are present in small numbers in all samples.

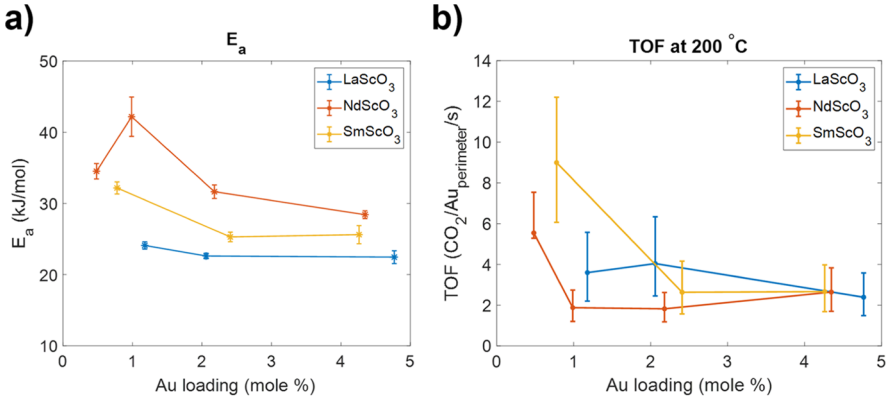


**Figure 4.** Activation energy of CO oxidation by Au on $LnScO_3$ (a) along with the TOFs at 200 °C (b). Arrhenius fits and the associated error bars in (a) were calculated from a linear least squares method and the errors in (b) were calculated using the standard deviations of the particle sizes.

nanoparticles are more sparsely distributed, the Au nanoparticles are far more mobile and prone to runaway (*i.e.*, unexpectedly significant) growth, yielding large, dewetted particles with a wide size distribution. Samples that underwent this runaway sintering finish the experiment with a smaller number of bigger particles after the catalytic cycling. In the case where the initial size is larger, the Au nanoparticles undergo more conventional sintering, and the particles remain similar to their initial morphologies in both shape and relative height (*i.e.*, truncated Wulff shapes at the surface rather than large Au polycrystals). We note that this is consistent with the standard size dependence of the chemical potential of nanoparticles.

We are deliberately not specifying the exact transition size between these two sintering regimes and the mechanism of sintering. Our data are too coarse to pin down an exact transition, and each support material should be treated separately because the strain at the interface is different for each support.

Turning now to the catalytic performance, Figure 4 shows the activation energies ($E_a$, calculated from rate data between 200 and 275 °C) and the turnover frequencies (TOFs) of the samples at 200 °C. The TOF is normalized to the number of perimeter Au atoms at the support interface per gram of the catalyst (this reaction is frequently modeled as an interfacial reaction[50,51]), calculated using sizes measured after catalytic cycling. Here, the highest energy barrier occurs at a given loading using $NdScO_3$ as the support, with that barrier decreasing moving to $SmScO_3$ and then $LaScO_3$. This exactly mirrors the trend in retained $CO_2$ on the support surfaces during TPD-MS measurements in the relevant temperature window. Turnover frequencies are less clear-cut but typically show the reaction proceeding slower over $NdScO_3$ at lower loadings. The samples with low loadings that underwent


https://doi.org/10.1021/acscatal.1c03156
ACS Catal. 2021, 11, 11921−11928

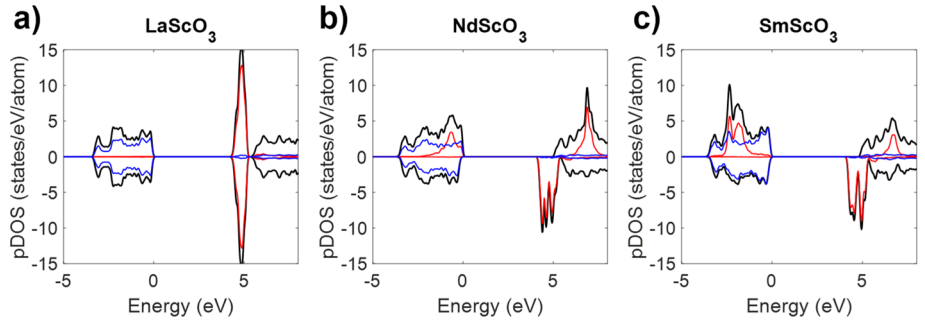


**Figure 5.** DOS of the $LnScO_3$ materials. Black lines represent the total DOS, while red lines represent the lanthanide 4f contribution with oxygen 2p in blue. In (a) $LaScO_3$ and (c) $SmScO_3$, the valence band edge consists of O 2p states, while in (b) $NdScO_3$, the Nd 4f states also sit at the edge.

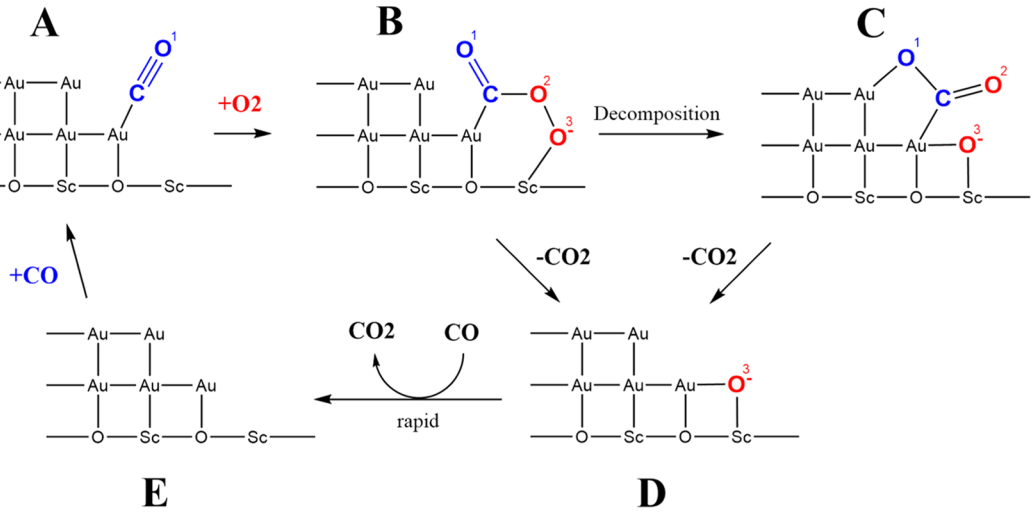


**Figure 6.** Proposed E−R reaction pathway for CO oxidation over $Au/LnScO_3$. CO bonds to Au (A) and then interacts with gaseous $O_2$ to form the $O^1CO^2O^3$ intermediate (B), then either decomposes to (C) before the desorption of $CO_2$ or moves directly to (D). The remaining $O^3$ atom (D) readily reacts with gaseous CO to refresh the catalyst surface (E).

runaway sintering were excluded from TOF calculations, and this is discussed further in Supporting Information. More details of the catalytic data are provided in Supporting Information, including rates calculated from the initial particle sizes, rate data at other temperatures, and Arrhenius plots used to calculate $E_a$. No notable differences in catalyst deactivation were noted between samples.

## DISCUSSION

There are many potential root causes behind varied activation energy and catalytic performance between two different materials; but in this experiment, owing to similarities across all samples, we have eliminated many of these. Looking first at the support surfaces, there is a common, Sc-rich double layer termination on the major pseudocubic facets. As a result, the catalytic performance is not affected by changes in the surface chemistry or symmetry that would occur, for instance, with different surface reconstructions or when using significantly different supports such as silica and titania. The lattice parameter changes linearly as we go from $LaScO_3$ to $NdScO_3$ then $SmScO_3$, which is different from the observed change in the activation energy and catalytic performance; hence, we can rule out here any major effect from the lattice parameter and epitaxial effects (in other systems, there is evidence for epitaxial contributions).[13,52−56] We note that this is consistent with the minimal change in the interfacial free energy mentioned earlier.

What does correlate well with the catalytic performance is that $NdScO_3$ is the most basic surface and binds $CO_2$ more strongly, followed by $SmScO_3$ and then $LaScO_3$ (when considering the temperature range of the catalytic experiments). In fact, $NdScO_3$ chemisorbs more $H_2O$ and $CO_2$ and has larger binding energy for $CO_2$, as shown in Figure 2b. The reason for this is almost certainly the 4f electrons on the Nd sites. In a previous analysis[30] of $DyScO_3$ and $TbScO_3$, it was apparent from both DFT calculations and XPS data that the minority 4f electrons were close to the Fermi energy, not at deep energies. This indicates that they are chemically active. Published XPS data[57,58] show a similar peak at the Fermi energy for $NdScO_3$, which correlates with the occupied portion of the bulk density of states (DOS), as shown in Figure 5b, which can be compared with those for $LaScO_3$ (no 4f electrons) and $SmScO_3$ (5 4f electrons), as shown in Figure 5a and Figure 5c, respectively; again the 4f electrons are chemically active.

This indicates that the Nd sites are less Lewis acidic due to the activity of the 4f electrons, that is, they are more able to donate electrons and increase the basicity of the overall system. We note that this will affect the chemisorption of species that accept electrons during the reaction process. The effect is not direct electron transfer from the lanthanide; rather, it is an inductive effect where the lanthanide 4f electrons affect the neighboring oxygen atoms, allowing them, in turn, to better donate charge. This trend is similar to the d-band theory as


https://doi.org/10.1021/acscatal.1c03156
ACS Catal. 2021, 11, 11921−11928

described by Hammer and Nørskov,[59] where a higher d-band center results in stronger adsorbate interaction, though notable differences exist (*e.g.*, d-band theory centers around the filling of antibonding states, and here, we point to the inductive effect associated with filled states). The impact of the f orbitals on adsorbate binding has not been raised before to our knowledge.

Specific reaction pathways for CO oxidation vary with the nature and reducibility of the support materials, specifically their ability to directly adsorb $O_2$ or create O vacancies through reduction. For example, theoretical work by Molina and Hammer shows CO oxidation with supported Au proceeding *via* an Eley−Rideal (E−R) mechanism on irreducible MgO[51] and a Langmuir−Hinshelwood pathway on $TiO_2$,[60] a reducible substrate. Additional studies with reducible supports such as $TiO_2$[61] and $CeO_2$[62] report that a Mars van Krevelen pathway is possible as a potential mechanism at higher temperatures. The supports studied herein are irreducible and therefore similar to MgO, with a basic surface, and we propose a similar E−R pathway pictured in Figure 6: CO binds to gold, then forms the intermediate oxidoperoxidocarbonate[63] species of $O^1CO^2O^3$[51,64−69] (we number the O atoms here and in the figure for discussion purposes only) with the assistance of electron donation from the substrate before the decomposition of the intermediate, then desorption of $CO_2$. This leads an active $O^3$ atom at the interface, as shown in Figure 6D, which can readily react with CO. The carbon of the intermediate is bonded to the gold, the negative end of the peroxide-type entity will be above one of the metal atoms at the support surface, herein scandium.

In this pathway, forming the interfacial $O^1CO^2O^3$ intermediate from CO bound to the metal and molecular $O_2$ involves charge transfer to the $O^3$ atom.[70,71] The inductive effect of the subsurface 4f electrons through the Sc double layer facilitates the charge transfer to the $O^3$ atom by increasing the activity of the electrons in the system. This reduces (more negative) the free energy of the transition state during the formation of the intermediate and also reduces the free energy of the $O^1CO^2O^3$ intermediate. This also increases the activation energy barrier for decomposition of the intermediate as the bond between the $O^2$ and $O^3$ atoms is strengthened.

The energetic barrier for this step is affected by the 4f inductive effect owing to the lowered energy of B compared to the subsequent steps in the reaction. The decomposed carbonate species in C is bonded to the metal, so it will not be lowered in energy by a strong inductive effect such as that on $NdScO_3$, and as a result, the energy barrier is larger due to the increased energy difference between B and C. The same effect is present moving straight from B to D. The 4f inductive effect stabilizes species at the interface, making it easier to form the intermediate state in B but harder to decompose it.

Though the inductive effect of the Nd 4f electrons hinders the reaction and creates a larger effective barrier for the case of CO oxidation over Au, this is not necessarily the case in all systems. Preliminary work using $Pt/LnScO_3$ shows the smallest apparent activation energy when using $NdScO_3$ as the support (to be published in detail soon, see Appendix III in Supporting Information), indicating that in systems where forming intermediates is the rate-limiting step, this effect can be leveraged to promote reactions.

## CONCLUSIONS

Considering the catalytic data and thorough characterization of both the support surfaces and catalytic nanoparticles, we determine that bonding of the reaction species at the metal−oxide interface in $Au/LnScO_3$ plays a critical role. In these systems, small changes to the Lewis acidity of the lanthanide due to the 4f electrons significantly affect charge transfer and lower the free energy of species bound to the interface.

## ASSOCIATED CONTENT

### Supporting Information

The Supporting Information is available free of charge at https://pubs.acs.org/doi/10.1021/acscatal.1c03156.

Quantified statistics of the Au size distributions, TOF results, and preliminary CO oxidation results with Pt (PDF)

## AUTHOR INFORMATION


### Corresponding Author

**Laurence D. Marks** − *Department of Materials Science and Engineering, Northwestern University, Evanston, Illinois 60208, United States;* orcid.org/0000-0002-6659-2016; Email: l-marks@northwerstern.edu

### Authors

**Zachary R. Mansley** − *Department of Materials Science and Engineering, Northwestern University, Evanston, Illinois 60208, United States;* orcid.org/0000-0002-1284-6316

**Ryan J. Paull** − *Department of Materials Science and Engineering, Northwestern University, Evanston, Illinois 60208, United States;* orcid.org/0000-0002-7273-7269

**Louisa Savereide** − *Department of Chemical and Biological Engineering, Northwestern University, Evanston, Illinois 60208, United States*

**Scott Tatro** − *Department of Chemical and Biological Engineering, Northwestern University, Evanston, Illinois 60208, United States*

**Emily P. Greenstein** − *Department of Materials Science and Engineering, Northwestern University, Evanston, Illinois 60208, United States*

**Abha Gosavi** − *Department of Chemical and Biological Engineering, Northwestern University, Evanston, Illinois 60208, United States;* orcid.org/0000-0002-1225-9082

**Emily Cheng** − *Department of Chemical and Biological Engineering, Northwestern University, Evanston, Illinois 60208, United States*

**Jianguo Wen** − *Center for Nanoscale Materials, Argonne National Laboratory, Lemont, Illinois 60439, United States;* orcid.org/0000-0002-3755-0044

**Kenneth R. Poeppelmeier** − *Department of Chemistry, Northwestern University, Evanston, Illinois 60208, United States;* orcid.org/0000-0003-1655-9127

**Justin M. Notestein** − *Department of Chemical and Biological Engineering, Northwestern University, Evanston, Illinois 60208, United States;* orcid.org/0000-0003-1780-7356

Complete contact information is available at: https://pubs.acs.org/10.1021/acscatal.1c03156


### Author Contributions

Support materials were synthesized by R.J.P. and E.P.G. with direction from K.R.P., and gold particles were deposited by A.G. Characterization experiments were performed by Z.R.M.

and E.C., with analysis by Z.R.M. and E.P.G. CO oxidation experiments were carried out by L.S. and S.T. with direction from J.M.N. Electronic structure calculations were performed by Z.R.M. and E.P.G. with assistance from L.D.M. The manuscript was principally written by Z.R.M. and L.D.M. and includes the contributions of all authors. All authors have given approval to the final version of the manuscript.

### Funding

This work was supported by the Northwestern University Institute for Catalysis in Energy Processes (ICEP) under grant no. DOE DE-FG02-03ER15457.

### Notes

The authors declare no competing financial interest.

## ■ ACKNOWLEDGMENTS

We acknowledge the use of the Center for Nanoscale Materials, a user facility at the Argonne National Lab supported by the U.S. Department of Energy, Office of Science, Office of Basic Energy Sciences, under contract no. DE-AC02-06CH11357.

## ■ REFERENCES

(1) Spenadel, L.; Boudart, M. Dispersion of Platinum on Supported Catalysts. *J. Phys. Chem.* **1960**, *64*, 204−207.
(2) Boudart, M. Catalysis by supported metals. *Adv. Catal.*. Academic Press, 1969; *20*, 153−166. DOI: 10.1016/s0360-0564(08)60271-0
(3) Boudart, M. Heterogeneous Catalysis by Metals. *J. Mol. Catal.* **1985**, *30*, 27−38.
(4) Wong, S.; Oteroschipper, P. H.; Wachter, W. A.; Inoue, Y.; Kobayashi, M.; Butt, J. B.; Burwell, R. L.; Cohen, J. B. Pt/Al2O3 II. Activity and selectivity patterns for methylcyclopropane hydrogenolysis and cyclopentane exchange with deuterium: Comparison with Pt/SiO2. *J. Catal.* **1980**, *64*, 84−100.
(5) Lewis, P. An X-Ray Absorption Edge Study of Zeolite-Supported Platinum. *J. Catal.* **1968**, *11*, 162−174.
(6) Comotti, M.; Li, W.-C.; Spliethoff, B.; Schüth, F. Support effect in high activity gold catalysts for CO oxidation. *J. Am. Chem. Soc.* **2006**, *128*, 917−924.
(7) Alexeev, O. S.; Chin, S. Y.; Engelhard, M. H.; Ortiz-Soto, L.; Amiridis, M. D. Effects of reduction temperature and metal-support interactions on the catalytic activity Pt/gamma-Al2O3 and Pt/TiO2 for the oxidation of CO in the presence and absence of H-2. *J. Phys. Chem. B* **2005**, *109*, 23430−23443.
(8) Park, E. D.; Lee, J. S. Effects of pretreatment conditions on CO oxidation over supported Au catalysts. *J. Catal.* **1999**, *186*, 1−11.
(9) Sankar, M.; He, Q.; Engel, R. V.; Sainna, M. A.; Logsdail, A. J.; Roldan, A.; Willock, D. J.; Agarwal, N.; Kiely, C. J.; Hutchings, G. J. Role of the Support in Gold-Containing Nanoparticles as Heterogeneous Catalysts. *Chem. Rev.* **2020**, *120*, 3890−3938.
(10) Kennedy, R. M.; Crosby, L. A.; Ding, K.; Canlas, C. P.; Gulec, A.; Marks, L. D.; Elam, J. W.; Marshall, C. L.; Poeppelmeier, K. R.; Stair, P. C. Replication of SMSI via ALD: TiO2 Overcoats Increase Pt-Catalyzed Acrolein Hydrogenation Selectivity. *Catal. Lett.* **2018**, *148*, 2223−2232.
(11) Tauster, S. J. Strong Metal-Support Interactions. *Accounts Chem. Res.* **1987**, *20*, 389−394.
(12) Enterkin, J. A.; Setthapun, W.; Elam, J. W.; Christensen, S. T.; Rabuffetti, F. A.; Marks, L. D.; Stair, P. C.; Poeppelmeier, K. R.; Marshall, C. L. Propane Oxidation over Pt/SrTiO3 Nanocuboids. *ACS Catal.* **2011**, *1*, 629−635.
(13) Enterkin, J. A.; Kennedy, R. M.; Lu, J.; Elam, J. W.; Cook, R. E.; Marks, L. D.; Stair, P. C.; Marshall, C. L.; Poeppelmeier, K. R. Epitaxial Stabilization of Face Selective Catalysts. *Top. Catal.* **2013**, *56*, 1829−1834.
(14) Zhang, Z.; Yates, J. T. Band Bending in Semiconductors: Chemical and Physical Consequences at Surfaces and Interfaces. *Chem. Rev.* **2012**, *112*, 5520−5551.
(15) Schlapka, A.; Lischka, M.; Gross, A.; Käsberger, U.; Jakob, P. Surface strain versus substrate interaction in heteroepitaxial metal layers: Pt on Ru(0001). *Phys. Rev. Lett.* **2003**, *91*, 016101.
(16) Yan, K.; Maark, T. A.; Khorshidi, A.; Sethuraman, V. A.; Peterson, A. A.; Guduru, P. R. The Influence of Elastic Strain on Catalytic Activity in the Hydrogen Evolution Reaction. *Angew. Chem. Int. Ed.* **2016**, *55*, 6175−6181.
(17) Lu, N.; Wang, X.; Suo, Z.; Vlassak, J. Failure by simultaneous grain growth, strain localization, and interface debonding in metal films on polymer substrates. *J. Mater. Res.* **2009**, *24*, 379−385.
(18) Komanicky, V.; Iddir, H.; Chang, K.-C.; Menzel, A.; Karapetrov, G.; Hennessy, D.; Zapol, P.; You, H. Shape-Dependent Activity of Platinum Array Catalyst. *J. Am. Chem. Soc.* **2009**, *131*, 5732−5733.
(19) Mann, A. K. P.; Wu, Z.; Calaza, F. C.; Overbury, S. H. Adsorption and Reaction of Acetaldehyde on Shape-Controlled CeO2 Nanocrystals: Elucidation of Structure-Function Relationships. *ACS Catal.* **2014**, *4*, 2437−2448.
(20) Foo, G. S.; Hu, G.; Hood, Z. D.; Li, M.; Jiang, D.-e.; Wu, Z. Kinetics and Mechanism of Methanol Conversion over Anatase Titania Nanoshapes. *ACS Catal.* **2017**, *7*, 5345−5356.
(21) Foo, G. S.; Hood, Z. D.; Wu, Z. Shape Effect Undermined by Surface Reconstruction: Ethanol Dehydrogenation over Shape-Controlled SrTiO3 Nanocrystals. *ACS Catal.* **2018**, *8*, 555−565.
(22) Uecker, R.; Bertram, R.; Brützam, M.; Galazka, Z.; Gesing, T. M.; Guguschev, C.; Klimm, D.; Klupsch, M.; Kwasniewski, A.; Schlom, D. G. Large-lattice-parameter perovskite single-crystal substrates. *J. Cryst. Growth* **2017**, *457*, 137−142.
(23) Uecker, R.; Velickov, B.; Klimm, D.; Bertram, R.; Bernhagen, M.; Rabe, M.; Albrecht, M.; Fornari, R.; Schlom, D. G. Properties of rare-earth scandate single crystals (Re = Nd-Dy). *J. Cryst. Growth* **2008**, *310*, 2649−2658.
(24) Koirala, P.; Mizzi, C. A.; Marks, L. D. Direct Observation of Large Flexoelectric Bending at the Nanoscale in Lanthanide Scandates. *Nano Lett.* **2018**, *18*, 3850−3856.
(25) Mizzi, C. A.; Koirala, P.; Gulec, A.; Marks, L. D. Charging ain't all bad: Complex physics in DyScO3. *Ultramicroscopy* **2019**, *203*, 119−124.
(26) Mansley, Z. R.; Mizzi, C. A.; Koirala, P.; Wen, J.; Marks, L. D. Structure of the (110) LnScO3 (Ln=Gd,Tb,Dy) surfaces. *Phys. Rev. Mater.* **2020**, *4*, 045003.
(27) Mansley, Z. R.; Paull, R. J.; Greenstein, E. P.; Wen, J.; Poeppelmeier, K. R.; Marks, L. D. ScOx Rich Surface Terminations on Lanthanide Scandate Nanoparticles, **2021**. Submitted
(28) Zhao, C.; Witters, T.; Brijs, B.; Bender, H.; Richard, O.; Caymax, M.; Heeg, T.; Schubert, J.; Afanas'ev, V. V.; Stesmans, A.; Schlom, D. G. Ternary rare-earth metal oxide high-k layers on silicon oxide. *Appl. Phys. Lett.* **2005**, *86*, 132903.
(29) Lim, S.-G.; Kriventsov, S.; Jackson, T. N.; Haeni, J. H.; Schlom, D. G.; Balbashov, A. M.; Uecker, R.; Reiche, P.; Freeouf, J. L.; Lucovsky, G. Dielectric functions and optical bandgaps of high-K dielectrics for metal-oxide-semiconductor field-effect transistors by far ultraviolet spectroscopic ellipsometry. *J. Appl. Phys.* **2002**, *91*, 4500−4505.
(30) Mizzi, C.; Koirala, P.; Marks, L. D. Electronic structure of lanthanide scandates. *Phys. Rev. Mater.* **2018**, *2*, 025001.
(31) Haruta, M.; Kobayashi, T.; Sano, H.; Yamada, N. Novel Gold Catalysts for the Oxidation of Carbon Monoxide at a Temperature far Below 0 °C. *Chem. Lett.* **1987**, *16*, 405−408.
(32) Paull, R. J.; Ly, T.; Mansley, Z. R.; Poeppelmeier, K. R.; Marks, L. D. Controlled Two-Step Formation of Faceted Perovskite Rare-Earth Scandate Nanoparticles. *Crystals* **2019**, *9*, 218.
(33) Paull, R. J.; Mansley, Z. R.; Ly, T.; Marks, L. D.; Poeppelmeier, K. R. Synthesis of Gadolinium Scandate from a Hydroxide Hydrogel. *Inorg. Chem.* **2018**, *57*, 4104−4108.

(34) Zanella, R.; Giorgio, S.; Shin, C. H.; Henry, C. R.; Louis, C. Characterization and reactivity in CO oxidation of gold nanoparticles supported on TiO2 prepared by deposition-precipitation with NaOH and urea. *J. Catal.* **2004**, *222*, 357−367.
(35) Blaha, P.; Schwarz, K.; Madsen, G. K. H.; Kvasnicka, D.; Luitz, J.; Laskowsji, R.; Tran, F.; Marks, L. D. *An Augmented Plane Wave + Local Orbitals Program for Calculating Crystal Properties*; Techn. Universitat Wien: Austria, 2018.
(36) Blaha, P.; Schwarz, K.; Tran, F.; Laskowski, R.; Madsen, G. K. H.; Marks, L. D. WIEN2k: An APW+lo program for calculating the properties of solids. *J. Chem. Phys.* **2020**, *152*, 074101.
(37) Novák, P.; Kuneš, J.; Chaput, L.; Pickett, W. E. Exact exchange for correlated electrons. *Phys. Status Solidi B* **2006**, *243*, 563−572.
(38) Tran, F.; Kuneš, J.; Novák, P.; Blaha, P.; Marks, L. D.; Schwarz, K. Force calculation for orbital-dependent potentials with FP-(L)APW plus lo basis sets. *Comput. Phys. Commun.* **2008**, *179*, 784−790.
(39) Perdew, J. P.; Ruzsinszky, A.; Csonka, G. I.; Vydrov, O. A.; Scuseria, G. E.; Constantin, L. A.; Zhou, X.; Burke, K. Restoring the density-gradient expansion for exchange in solids and surfaces. *Phys. Rev. Lett.* **2008**, *100*, 136406.
(40) Dirsyte, R.; Schwarzkopf, J.; Wagner, G.; Fornari, R.; Lienemann, J.; Busch, M.; Winter, H. Thermal-induced change in surface termination of DyScO3(110). *Surf. Sci.* **2010**, *604*, L55−L58.
(41) Kleibeuker, J. E.; Koster, G.; Siemons, W.; Dubbink, D.; Kuiper, B.; Blok, J. L.; Yang, C.-H.; Ravichandran, J.; Ramesh, R.; ten Elshof, J. E.; Blank, D. H. A.; Rijnders, G. Atomically Defined Rare-Earth Scandate Crystal Surfaces. *Adv. Funct. Mater.* **2010**, *20*, 3490−3496.
(42) Kleibeuker, J. E.; Kuiper, B.; Harkema, S.; Blank, D. H. A.; Koster, G.; Rijnders, G.; Tinnemans, P.; Vlieg, E.; Rossen, P. B.; Siemons, W.; Portale, G.; Ravichandran, J.; Szepieniec, J. M.; Ramesh, R. Structure of singly terminated polar DyScO3 (110) surfaces. *Phys. Rev. B: Condens. Matter Mater. Phys.* **2012**, *85*, 165413.
(43) Biswas, A.; Yang, C.-H.; Ramesh, R.; Jeong, Y. H. Atomically flat single terminated oxide substrate surfaces. *Prog. Surf. Sci.* **2017**, *92*, 117−141.
(44) Marks, L. D.; Smith, D. J. High-Resolution Studies of Small Particles of Gold and Silver. I. Multiply-Twinned Particles. *J. Cryst. Growth* **1981**, *54*, 425−432.
(45) Smith, D. J.; Marks, L. D. High-Resolution Studies of Small Particles of Gold and Silver. II. Single-Crystals, Lamellar Twins and Polyparticles. *J. Cryst. Growth* **1981**, *54*, 433−438.
(46) Marks, L. D. Experimental Studies of Small-Particle Structures. *Rep. Prog. Phys.* **1994**, *57*, 603−649.
(47) Marks, L. D.; Peng, L. Nanoparticle shape, thermodynamics and kinetics. *J. Phys. Condens. Matter* **2016**, *28*, 053001.
(48) Winterbottom, W. L. Equilibrium shape of a small particle in contact with a foreign substrate. *Acta Metall.* **1967**, *15*, 303−310.
(49) Mansley, Z. R.; Marks, L. D. Modified Winterbottom Construction Including Boundaries. *J. Phys. Chem. C* **2020**, *124*, 28038−28043.
(50) Meyer, R.; Lemire, C.; Shaikhutdinov, S. K.; Freund, H.-J. Surface chemistry of catalysis by gold. *Gold Bull.* **2004**, *37*, 72−124.
(51) Molina, L. M.; Hammer, B. Active role of oxide support during CO oxidation at Au/MgO. *Phys. Rev. Lett.* **2003**, *90*, 206102.
(52) Jalan, V.; Taylor, E. J. Importance of Interatomic Spacing in Catalytic Reduction of Oxygen in Phosphoric-Acid. *J. Electrochem. Soc.* **1983**, *130*, 2299−2302.
(53) Kampshoff, E.; Hahn, E.; Kern, K. Correlation between Surface Stress and the Vibrational Shift of Co Chemisorbed on Cu Surfaces. *Phys. Rev. Lett.* **1994**, *73*, 704−707.
(54) Khorshidi, A.; Violet, J.; Hashemi, J.; Peterson, A. A. How strain can break the scaling relations of catalysis. *Nat. Catal.* **2018**, *1*, 263−268.
(55) Gsell, M.; Jakob, P.; Menzel, D. Effect of substrate strain on adsorption. *Science* **1998**, *280*, 717−720.
(56) Escudero-Escribano, M.; Malacrida, P.; Hansen, M. H.; Vej-Hansen, U. G.; Velazquez-Palenzuela, A.; Tripkovic, V.; Schiotz, J.; Rossmeisl, J.; Stephens, I. E. L.; Chorkendorff, I. Tuning the activity of Pt alloy electrocatalysts by means of the lanthanide contraction. *Science* **2016**, *352*, 73−76.
(57) Haasch, R. T.; Breckenfeld, E.; Martin, L. W. An Introduction to Single Crystal Perovskites and Single Crystal Rare-Earth Scandate Perovskites Analyzed Using X-ray Photoelectron Spectroscopy. *Surf. Sci. Spectra* **2014**, *21*, 84−86.
(58) Haasch, R. T.; Martin, L. W.; Breckenfeld, E. Single Crystal Rare-earth Scandate Perovskites Analyzed Using X-ray Photoelectron Spectroscopy: 2. NdScO3(110). *Surf. Sci. Spectra* **2014**, *21*, 140−148.
(59) Hammer, B.; Norskov, J. K. Why Gold Is the Noblest of All the Metals. *Nature* **1995**, *376*, 238−240.
(60) Molina, L. M.; Rasmussen, M. D.; Hammer, B. Adsorption of O-2 and oxidation of CO at Au nanoparticles supported by TiO2(110). *J. Chem. Phys.* **2004**, *120*, 7673−7680.
(61) Schlexer, P.; Widmann, D.; Behm, R. J.; Pacchioni, G. CO Oxidation on a Au/TiO2 Nanoparticle Catalyst via the Au-Assisted Mars-van Krevelen Mechanism. *ACS Catal.* **2018**, *8*, 6513−6525.
(62) Kim, H. Y.; Lee, H. M.; Henkelman, G. CO Oxidation Mechanism on CeO2-Supported Au Nanoparticles. *J. Am. Chem. Soc.* **2012**, *134*, 1560−1570.
(63) PubChem Compound Summary for CID 5460578 *Oxidoperoxidocarbonate(.1-)*. National Center for Biotechnology Information, 2021.
(64) Hagen, J.; Socaciu, L. D.; Elijazyfer, M.; Heiz, U.; Bernhardt, T. M.; Wöste, L. Coadsorption of CO and O-2 on small free gold cluster anions at cryogenic temperatures: Model complexes for catalytic CO oxidation. *Phys. Chem. Chem. Phys.* **2002**, *4*, 1707−1709.
(65) Liu, Z.-P.; Hu, P.; Alavi, A. Catalytic role of gold in gold-based catalysts: A density functional theory study on the CO oxidation on gold. *J. Am. Chem. Soc.* **2002**, *124*, 14770−14779.
(66) Jiang, Q.; Zhang, J.; Ao, Z.; Huang, H.; He, H.; Wu, Y. First Principles Study on the CO Oxidation on Mn-Embedded Divacancy Graphene. *Front. Chem.* **2018**, *6*, 187.
(67) Huber, H.; Mcintosh, D.; Ozin, G. A. Metal Atom Model for Oxidation of Carbon-Monoxide to Carbon-Dioxide - Gold Atom Carbon Monoxide Dioxygen Reaction and Gold Atom Carbon Dioxide Reaction. *Inorg. Chem.* **1977**, *16*, 975−979.
(68) Tang, D.; Zhang, J. Theoretical investigation on CO oxidation catalyzed by a copper nanocluster. *RSC Adv.* **2013**, *3*, 15225−15236.
(69) Davran-Candan, T.; Demir, M.; Yildirim, R. Analysis of reaction mechanisms and kinetics of preferential CO oxidation over Au/gamma-$Al_2O_3$. *React. Kinet. Mech. Catal.* **2011**, *104*, 389−398.
(70) Falsig, H.; Hvolbæk, B.; Kristensen, I. S.; Jiang, T.; Bligaard, T.; Christensen, C. H.; Nørskov, J. K. Trends in the catalytic CO oxidation activity of nanoparticles. *Angew. Chem. Int. Ed.* **2008**, *47*, 4835−4839.
(71) Hammer, B. Special sites at noble and late transition metal catalysts. *Top. Catal.* **2006**, *37*, 3−16.


https://doi.org/10.1021/acscatal.1c03156
*ACS Catal.* 2021, 11, 11921−11928